https://doi.org/10.1016/j.cej.2021.131512

Article type: Full Paper

Carbon-Mediated Electron Transfer Channel between SnO_2 QDs and g-C_3N_4 for Enhanced Photocatalytic H_2 Production

Jia Yan,[a] Zhilong Song,[b] Hongping Li,[b] Hui Xu,[b,*] and Lawrence Yoon Suk Lee[a,c,*]

[a] Department of Applied Biology and Chemical Technology and State Key Laboratory of Chemical Biology and Drug Discovery, The Hong Kong Polytechnic University, Hung Hom, Kowloon, Hong Kong SAR, China.

[b] Institute for Energy Research, Jiangsu University, Zhenjiang, Jiangsu 212013, China.

[c] Research Institute for Smart Energy, The Hong Kong Polytechnic University, Hung Hom, Kowloon, Hong Kong SAR, China.

* E-mails: xh@ujs.edu.cn (H. Xu), lawrence.ys.lee@polyu.edu.hk (L. Y. S. Lee)

Keywords: SnO_2 quantum dots; g-C_3N_4 nanosheets; carbon encapsulation; electron transport layer; photocatalytic hydrogen production

Graphical abstract

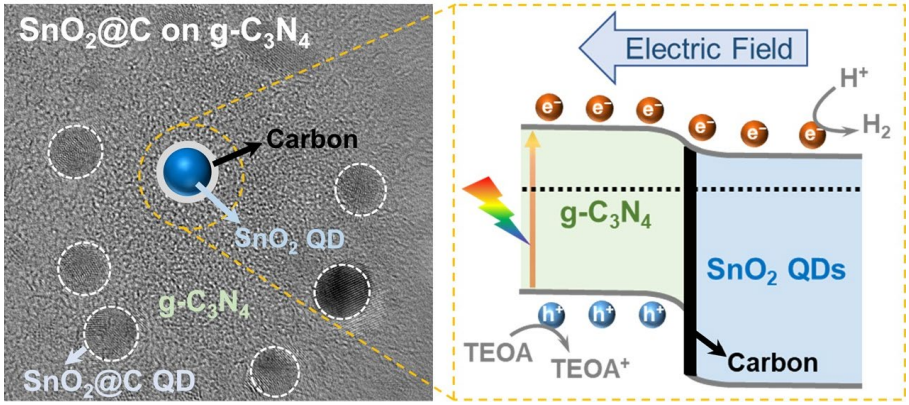

Abstract

Graphitic carbon nitride (g-C_3N_4) is a promising material for photocatalytic water splitting but suffers from the self-agglomeration and fast recombination of photogenerated electron–hole pairs. Tin oxide (SnO_2) has a high electron extraction ability and can play a key role in the charge separation and transfer dynamics of composites. Herein, we report a 0D/2D heterostructure of carbon-encapsulated SnO_2 quantum dots (SnO_2@C QDs) anchored on g-C_3N_4 nanosheets (SnO_2@C/CN). The construction of interface between SnO_2@C and g-C_3N_4 dramatically increases the surface area and the number of active sites for photocatalytic hydrogen evolution reaction (HER) and provides a driving force for efficient charge separation/transfer kinetics. The carbon layer encapsulating SnO_2 QDs acts as a bridge that facilitates electron transfer from g-C_3N_4 to SnO_2 QDs. The champion SnO_2@C/CN achieves an exceptional HER rate of 2,544.3 μmol g^{-1} h^{-1} (with 3 wt.% Pt) with an apparent quantum efficiency of 9.63 % (λ = 420 nm) and excellent photostability. A photoactivity enhancement mechanism is proposed based on the interfacial energy band alignment. This work provides insights into the designing of heterostructured photocatalysts of enhanced charge separation *via* interface engineering.

1. Introduction

Graphitic carbon nitride (g-C_3N_4) has drawn much attention as a metal-free photocatalyst for hydrogen evolution reaction (HER) owing to its low cost, abundant raw material supply, easy production, good visible light response, and suitable conduction band [1, 2]. However, pristine g-C_3N_4 shows only limited performances in photocatalytic HER due to its fast charge recombination and easy agglomeration [3]. Tremendous effort has been devoted to addressing these drawbacks, and the constructing of a heterostructure provides one of the potential solutions [4-8]. The interface between two dissimilar components of heterostructures can facilitate charge separation and transfer in a specific direction, suppressing undesired processes such as charge recombination [9-11]. The energy level alignment between two semiconductors of dissimilar band structures can induce interfacial electron separation and transfer, which could lead to the modulation of electronic structure at the interface to favor desired photocatalytic activities [12]. Moreover, the photogenerated electrons would migrate to align the Fermi levels of the two components at the interface, inducing a band bending that creates an internal electric field in the space charge region [13]. This also provides a driving force for the separation and transportation of photo-induced charges at the interface, which is beneficial for enhancing photocatalytic HER efficiency. Therefore, it is highly imperative to promote photocarrier transfer kinetics by constructing a g-C_3N_4-based heterostructure with a suitable semiconductor to develop advanced HER photocatalysts [14-16].

Tin oxide (SnO_2) is a promising candidate for constructing heterostructured catalytic systems because of its suitable band positions and large charge mobility. For these advantages, SnO_2 has attracted much attention from various research fields including Li-ion batteries [17,

18], electrochemical capacitors [19], perovskite solar cells [20-23], gas sensors [24-26], and N_2 reduction [27]. In a heterostructure, SnO_2 can act as an electron sink and attract photoelectrons from another semiconductor, which can improve the separation and transfer of charge carriers [28, 29]. Previous studies reported enhanced separation efficiencies of photogenerated electron–hole pairs at the interface between SnO_2 and g-C_3N_4 in the applications of photocatalytic dye degradation [30-33], CO_2 reduction [34], and HER [35]. Such SnO_2/g-C_3N_4 photocatalysts, however, still show limited utilization of visible light, and their loosely packed morphologies provide insufficient surface area, consequently resulting in low catalytic efficiencies.

Recently, heterostructures of zero/two-dimensional (0D/2D) materials, especially quantum dots (QDs)/nanosheets (NSs) heterostructures, have aroused intense interest as an ideal composite structure of high charge mobility, which allows effective use of photoexcited electrons/holes [36-38]. Compared with SnO_2 nanoparticles, SnO_2 QDs of several nanometer diameters possess excellent photoelectronic properties, efficient adsorption capacity, and high chemical activity stemming from their high surface-to-volume ratio, internal and surface defects, and strong quantum confinement effect [27, 39, 40]. However, the prevention of SnO_2 QDs' self-aggregation while enhancing their light absorption capacity remains a challenge. Carbon encapsulation has been suggested as an effective strategy to address such problems. A thin layer of carbon can act as a chemically stable surface, preventing the nanocrystals from oxidization and aggregation. For instance, a perovskite encapsulated with graphite sheet showed good stability during water oxidation reaction [41, 42]. Besides, carbon encapsulation can also serve as a solid-state mediator that accelerates the charge carrier at the interface of the

heterojunctions as demonstrated by carbon-encapsulated WO_x on carbon support [43] and reduced graphene oxide-covered perylene diimide polymer on carbon nitride support [44].

Herein, we report carbon-encapsulated SnO_2 QDs anchored on g-C_3N_4 nanosheets (SnO_2@C/CN) that show a high photocatalytic activity toward HER. Theoretical calculations reveal that carbon encapsulation can stabilize the SnO_2 QDs and strengthen the interaction between SnO_2 QDs and g-C_3N_4 nanosheets. An internal electric field thus formed at the intimate interface between SnO_2 QDs and g-C_3N_4 promotes the separation and one-directional migration of photogenerated charges. As a result, the optimized SnO_2@C/CN heterostructure achieves an exceptional H_2 evolution rate of 2,544.3 μmol h^{-1} g^{-1}, which is 5 times higher than that of the pristine g-C_3N_4, with an apparent quantum efficiency of 9.63 % at λ = 420 nm.

2. Experimental section

2.1. Chemicals

Tin (IV) chloride pentahydrate ($SnCl_4 \cdot 5H_2O$, 98%), oleic acid (OA, 99%), oleylamine (OLA, 80-90%), methanol (99.5%), and thiourea (99%) were purchased from Sigma Aldrich. All chemicals were used without further treatment.

2.2. Preparation of SnO_2 QDs, SnO_2@C/CN, and SnO_2@C NSs

A colloidal method was adopted for the synthesis of SnO_2 QDs. Briefly, $SnCl_4 \cdot 5H_2O$ (0.6 g) was dispersed in a mixture of oleic acid (OA, 22.5 mL) and oleylamine (OLA, 2.5 mL) and sonicated for 10 min, followed by the addition of methanol (10 mL). The mixture was transferred to a 50 mL Teflon-lined stainless-steel autoclave and heated to 180 °C for 3 h. The

as-obtained SnO_2 QDs were washed with methanol and hexane several times and finally dispersed in 20 mL methanol.

Thiourea (1 g) was added to the methanolic dispersion of SnO_2 QDs (15 mg mL^{-1}) under magnetic stirring for 1 h. After oven-drying at 60 °C for 6 h, the mixture was annealed in a tube furnace at 550 °C for 4 h with a heating rate of 2 °C min^{-1} under Ar flow. The product was cooled down to room temperature and ground to yield a SnO_2@C/CN composite as a dark brown powder. The amount of SnO_2 QDs solution added to the reaction mixture was 4, 6, or 8 mL, and the corresponding SnO_2@C/CN composites were named as SnO_2@C/CN-1, SnO_2@C/CN-2, and SnO_2@C/CN-3, respectively. For comparison, g-C_3N_4 and carbon-encapsulated SnO_2 nanosheets (SnO_2@C NSs) were prepared using the same procedure in the absence of SnO_2 QDs or thiourea.

2.3. Material characterizations

The morphology of the as-prepared samples was analyzed using a field emission scanning electron microscope (FE-SEM, JEOL JSM-7800F) and a high-resolution transmission electron microscope (HRTEM, JEOL JEM-2100 F) operated at 300 kV. The samples for HRTEM analysis were prepared by drop-casting the as-prepared samples that were dispersed in ethanol onto a holey carbon-coated 400 mesh Cu TEM grid. Elemental analyses were conducted using the energy-dispersive X-ray spectroscopy (EDX) equipped on the TEM system. Structural information was acquired by X-ray diffraction (XRD) on a Bruker D8 diffractometer employing Cu Kα radiation (λ = 1.5418 Å). Fourier-transform infrared spectra (FT-IR) were collected with a Fourier-transform spectrophotometer (Nexus 470, Thermo Electron Corporation) using a standard KBr disk. Thermal gravimetric analyses (TGA) were performed

on a TGA/DSC3+ analyzer (Mettler Toledo Instruments Inc.) at temperatures ranging from room temperature to 800 °C at a ramp rate of 10 °C min^{-1} under nitrogen (N_2) flow. X-ray photoelectron spectroscopy (XPS) was conducted on an ESCALAB 250Xi X-ray photoelectron spectrometer (Thermo Fisher) with a monochromic Al Kα X-ray source and a pass energy of 1486.6 eV. On the same instrument, work functions were confirmed using ultraviolet photoelectron spectroscopy (UPS) with the excitation energy of He I (21.22 eV). UV–vis diffuse reflectance spectra (DRS) were taken using a Cary 4000 UV–vis spectrophotometer and $BaSO_4$ was used as the reflectance standard. Photoluminescence (PL) spectra were obtained on an FLS1000 fluorescence spectrophotometer (Edinburgh Instruments) with an excitation wavelength of 325 nm. Time-resolved PL (TRPL) decay curves were recorded on the same spectrophotometer with a 325 nm pulsed laser. The obtained decay curves were fitted based on the exponential kinetic function equation (1) [38]:

$$I(t) = A_1 \times \exp(-t/\tau) \quad (1)$$

where A_1 is the corresponding amplitudes and τ denotes the decay time.

2.4. Electrochemical measurements

Photocurrent measurements and electrochemical impedance spectroscopy (EIS) were conducted on an electrochemical workstation (Interface 1000E, Gamry Instrument) using a three-electrode system. A saturated Ag/AgCl electrode and a Pt wire were used as the reference and counter electrodes, respectively. Catalyst ink was prepared by dispersing the as-prepared sample (1 mg) in a mixture of ethanol (250 μL) and deionized water (750 μL), followed by sonication for 30 min. The ink (20 μL) was drop-cast onto an indium-tin oxide glass (ITO, 0.5 × 1 cm^2) and used as the working electrode. Na_2SO_4 solution (0.1 M) was used as an electrolyte

for photocurrent measurements. The EIS study was conducted in the frequency range from 100 kHz to 0.01 Hz with an amplitude of 5 mV at open circuit potential.

2.5. Photocatalytic H_2 Evolution

Photocatalytic H_2 evolution reaction was carried out in an on-line photocatalytic analysis system (Labsolar-IIIAG, Beijing PerfectLight). The as-prepared catalyst (10 mg) was dispersed in an aqueous solution (100 mL) of triethanolamine (TEOA, 10 %), and 3 wt.% Pt was *in situ* photo-deposited as a co-catalyst. After degassing by bubbling Ar for 30 min, the suspended solution was irradiated with a 300 W Xenon lamp (PLS-SXE 300C (BF), PerfectLight) equipped with an optical filter (λ > 400 nm). The reaction product in the headspace was periodically sampled with a gas tight syringe and analyzed by an online gas chromatograph (GC D7900P, TCD detector, N_2 carrier, 5A molecular sieve column, Shanghai Fechcomp). Apparent quantum efficiency (AQE) of H_2 production was measured using a 300 W Xenon lamp with a filter (λ = 420, 425, 435, 475, and 550 nm) and calculated based on the following equation:

$$\text{AQE} = 2 \times \frac{\text{number of } H_2 \text{ molecules produced}}{\text{number of incident photons}} \times 100\ \% \qquad (2)$$

3. Results and Discussion

Scheme 1 illustrates the preparation procedure of SnO_2 quantum dots (QDs), carbon-encapsulated SnO_2 nanosheets (SnO_2@C NSs), and a heterostructure composed of carbon-encapsulated SnO_2 QDs anchored on g-C_3N_4 nanosheets (SnO_2@C/CN). The SnO_2 QDs were synthesized *via* a colloidal method in the presence of oleic acid (OA) and oleylamine (OLA).

The surface of the as-obtained SnO_2 QDs is capped with long alkylchains of OA and OLA, which prevent the agglomeration of the SnO_2 QDs and render them solution-processable [45]. The subsequent calcination at 550 °C yields SnO_2@C NSs. During the calcination process, the OA and OLA on the SnO_2 QD surface are first decomposed (boiling points of OA and OLA = *ca.* 360 °C) to form an amorphous carbon layer that prevents the aggregation and further growth of the SnO_2 QDs. As the calcination temperature approaches 550 °C, the carbon decomposition and the collision contacts of the SnO_2 QDs are accelerated, which result in a continuous growth of the SnO_2 QDs to amorphous carbon-encapsulated SnO_2 NSs as verified by scanning electron microscopic (SEM) and transition electron microscopic (TEM) images (**Fig. S1a** and **S1b**). A high-degree crystallinity of the SnO_2@C NS is confirmed by a high-resolution TEM (HRTEM, **Fig. S1c**) image that displays clear lattice fringes with interplanar spacings of 0.334 and 0.267 nm corresponding to the (110) and (101) planes of rutile SnO_2 (JCPDS# 41-1445) [17], respectively.

On the other hand, the calcination of SnO_2 QDs in the presence of thiourea affords a distinct nanocomposite of carbon-encapsulated SnO_2 QDs and g-C_3N_4 nanosheets. When mixed with the as-prepared SnO_2 QDs, thiourea acts as a short-chain ligand that partially replaces the surface-bound OA and OLA. Fourier-transform infrared spectra (FT-IR) shown in **Fig. S2** confirm the partial ligand exchange on the surface of the SnO_2 QDs that are mixed with various amounts of thiourea for 1h. The as-prepared SnO_2 QDs display C–H stretching vibrations of OA/OLA at 2,926 and 2,854 cm^{-1} [46], which gradually decrease with the introduction of thiourea. Simultaneously, a characteristic C=S vibration peak appears at 735 cm^{-1} [47], which confirms the partial replacement of OA/OLA with thiourea. During the calcination process,

thiourea condenses and assembles to 2D g-C_3N_4, providing active sites for the SnO_2 QDs to anchor [48], while the surface-capped OA and OLA are decomposed to amorphous carbon and coated on the surface of the SnO_2 QDs, resulting in the formation of a 0D/2D SnO_2@C/CN heterostructure. The SnO_2 QDs-to-thiourea mass ratio used are 6:100, 9:100, and 12:100, and the calcination products were named as SnO_2@C/CN-1, SnO_2@C/CN-2, and SnO_2@C/CN-3, respectively.

X-ray diffraction (XRD) spectra of the as-prepared SnO_2 QDs, g-C_3N_4, and SnO_2@C/CN heterostructures were collected to investigate their crystal phase and purity (**Fig. 1a**). The g-C_3N_4 nanosheets show two characteristic peaks; a minor peak at 13.1° is assigned to the (100) plane that represents the in-plane structural repeating motifs of heptazine units, while the strong one at 27.4° corresponds to the (002) crystal plane of π–π interlayer stacking [49]. The SnO_2 QDs display diffraction peaks at 26.6°, 33.9°, 37.9°, 51.8°, 57.8°, and 64.7°, which are indexed to the (110), (101), (200), (211), (002), and (112) planes of rutile SnO_2 (JCPDS# 41-1445), respectively [17]. The SnO_2@C/CN samples display similar XRD patterns to that of the pristine SnO_2, indicating the rutile structure is retained. It is worth noting that the peak intensities increase from SnO_2@C/CN-1 to SnO_2@C/CN-3, which agrees with the amount of SnO_2 QDs used. No obvious peaks for g-C_3N_4 are observable from the XRD patterns of SnO_2@C/CN samples as the characteristic (002) peak of g-C_3N_4 (27.4°) overlaps the (110) peak of SnO_2 QDs (26.6°). The FT-IR spectra of the SnO_2@C/CN samples (**Fig. 1b**), however, indicate the presence of g-C_3N_4 with the sharp absorption peak at 809 cm^{-1}, which is attributed to the bending vibration mode of *s*-triazine units of g-C_3N_4. In addition, strong vibration peaks located at 1,230~1,640 cm^{-1} are ascribed to the stretching vibrations of aromatic C–N and C=N

heterocycles, while the broad peak between 3,000 and 3,600 cm^{-1} corresponds to the stretching vibration of the N–H band [50]. The intensity of the peak at 809 cm^{-1} decreases from SnO_2@C/CN-1 to SnO_2@C/CN-3, which is consistent with the XRD observations. The pristine SnO_2 QDs exhibit the characteristic peaks for the stretching vibrations of Sn–O bonds at 489 and 681 cm^{-1} [49] as well as the C−H stretching vibrations of OA/OLA at 2,926 and 2,854 cm^{-1} [46] without any g-C_3N_4-related peaks.

The morphologies of g-C_3N_4, SnO_2 QD, and SnO_2@C/CN samples were examined using SEM and TEM. **Fig. 2a** shows the TEM image of highly crystalline SnO_2 QDs (average diameter = *ca.* 3.6 nm) which reveals the lattice fringes. The interplanar spacings of *ca*. 0.334 and 0.267 nm correspond to the (110) and (101) planes of the rutile SnO_2 [49], which is in good accordance with the XRD results. The TEM image of g-C_3N_4 (**Fig. S1d**) indicates a typical 2D layered-nanosheet structure in large lateral sizes. The SEM images in **Fig. S3** compare the morphologies of the SnO_2@C/CN composites. Among the three SnO_2@C/CN composites, SnO_2@C/CN-2 shows the most obvious layered structure with the largest lateral size (**Fig. S3a–S3c**). The corresponding TEM images (**Fig. S3d–S3f**) disclose the agglomeration of SnO_2@C/CN-1 and SnO_2@C/CN-3 because of either excessive or insufficient formation of g-C_3N_4. It is crucial to balance the amount of SnO_2 QDs and thiourea to stabilize SnO_2 QDs in the layer-structured g-C_3N_4.

Fig. 2b shows a typical SnO_2@C/CN-2 heterostructure where the SnO_2@C are uniformly dispersed on the surface of 2D g-C_3N_4 nanosheet. The unchanged lattice spacings of SnO_2 QDs indicate their crystal structure is preserved during the calcination process. The amorphous carbon layers encapsulating the SnO_2 QDs are visible, although it is difficult to distinguish

them from g-C_3N_4 due to similar morphologies. Energy-dispersive X-ray (EDX) elemental mapping images (**Fig. 2c**) unveil the homogeneous distribution of C, N, Sn, and O elements, confirming the successful construction of the SnO_2@C/CN heterostructure.

Fig. 2d and **2e** illustrate the optimized adsorption configurations of bare SnO_2 and SnO_2@C QDs on g-C_3N_4 surface. The coordination environments and frameworks of the optimized bare SnO_2 and SnO_2@C QDs are retained after the adsorption on g-C_3N_4 (**Fig. S4**). The simulations indicate that g-C_3N_4 nanosheet is, however, dramatically deformed by the interaction with bare SnO_2 and SnO_2@C QDs as it tends to afford as many adsorption sites as possible. The adsorption energy (E_{ads}, **Table S1**) between g-C_3N_4 and SnO_2@C QD is calculated to be −532.2 kcal mol^{-1}, which is higher than that of bare SnO_2 QD (−444.4 kcal mol^{-1}). These results clearly demonstrate the role of amorphous carbon layer in stabilize SnO_2 QDs and strengthening the interaction between SnO_2 QDs and g-C_3N_4 nanosheet.

Thermogravimetric analysis (TGA) was carried out to determine the amount of SnO_2 QDs in the SnO_2@C/CN composites (**Fig. S5**). The g-C_3N_4 completely decomposes at >700 °C in N_2, whereas SnO_2@C/CN-1, SnO_2@C/CN-2, and SnO_2@C/CN-3 exhibit residual masses of *ca*. 31.3, 39.4, and 46.7 % at 800 °C, respectively, which indicate the SnO_2 QD contents in the composites. Meanwhile, a mixture of OA and OLA (mass ratio = 9:1) was also analyzed by TGA to quantify the amount of carbon encapsulation in SnO_2@C (**Fig. S6a**). The evaporation and decomposition of OA and OLA cause a rapid mass loss between 200 and 350 °C and about 2.7 % of the mass remains at 550 °C, which can be attributed to the vestigial carbon. The color of the mixture changes from translucent to black after calcination at 550 °C under N_2 flow (**Fig. S6b**), confirming the conversion of OA and OLA to carbon.

The effects of carbon encapsulation on the specific surface area and porosity were studied by comparing the N_2 adsorption–desorption isotherms of SnO_2 QDs, g-C_3N_4, and SnO_2@C/CN composites as presented in **Fig. S7**. The SnO_2 QDs exhibit a type IV isotherm and H2 type hysteresis loop (**Fig. S7a**), reflecting their uniform pore size distribution. All the isotherms and hysteresis loops of g-C_3N_4 and SnO_2@C/CN composites (**Fig. S7b–S7e**) can be ascribed to type IV and type H3, respectively, which indicate the existence of slit-shaped mesopores in the self-assembled flakes. The pore width distribution curves obtained by the Barret−Joyner−Halenda (BJH) method confirm the presence of abundant mesopores (**Fig. S7f**) that are beneficial for mass transfer kinetics. The BET specific surface area of SnO_2 QDs, g-C_3N_4, SnO_2@C/CN-1, SnO_2@C/CN-2, and SnO_2@C/CN-3 is 84.0, 17.9, 27.6, 48.2, and 38.9 $m^2\ g^{-1}$, respectively. It is noteworthy that the specific surface area and mesopore volume are increased by anchoring the SnO_2@C on g-C_3N_4 surface, providing more active sites for heterogeneous catalysis. The SnO_2@C/CN-3 exhibits a lower BET specific surface area than SnO_2@C/CN-2 due to agglomeration caused by insufficient formation of g-C_3N_4 (**Fig. S3c** and **S3f**).

X-ray photoelectron spectroscopy (XPS) was employed to understand the interfacial interactions between the SnO_2@C and g-C_3N_4. XPS survey spectra (**Fig. S8**) confirm the presence of Sn, O, C, and N elements in the SnO_2@C/CN-2 heterostructure with no other impurities identified. The high-resolution Sn 3d spectrum of SnO_2@C/CN-2 (**Fig. 3a**) exhibits two spin-orbital ($2d_{5/2}$ and $2d_{3/2}$) peaks at 487.10 and 495.51 eV, which are shifted from the lower binding energies of 486.77 and 495.20 eV in SnO_2 QDs, respectively [51]. Similar positive shifts are observed from the O–Sn and C–O peaks in the O 1s and C 1s core-level

spectra, respectively (top and middle panels in **Fig. 3b** and **3c**). On the contrary, the binding energy of O–C in the pristine g-C_3N_4 (532.17 eV) decreases in SnO_2@C/CN-2 (531.70 eV), while the binding energy of π excitation in the N 1s core-level spectra increases when g-C_3N_4 (405.36 eV) is conjugated with SnO_2@C (405.94 eV, **Fig. 3d**). The binding energy shift arises from the interaction between the Coulomb forces of the inner electrons and the shielding effect of the outer electrons, and higher outer electron density would lead to lower binding energy and *vice versa* [52]. Therefore, it is reasonable to conclude that the binding energy shifts observed upon the formation of the SnO_2@C/CN heterostructure are caused by the electron transfer from SnO_2@C QDs to g-C_3N_4, and the encapsulating carbon on SnO_2 QDs is believed to accelerate the electron transfer to g-C_3N_4. Such strong electron coupling can contribute to the formation of an internal electric field that can facilitate the charge carrier separation/transfer efficiency.

Photocurrent measurement can provide more insights into the photogenerated electron transfer behavior. **Figs. 4a** compares the photocurrent responses of SnO_2@C/CN samples and g-C_3N_4, where the SnO_2@C/CN-1, SnO_2@C/CN-2, and SnO_2@C/CN-3 show the on/off ratios that are 1.4, 2.3, and 1.7 times higher than that of pristine g-C_3N_4, respectively. This clearly demonstrates a promoted surface reaction kinetics as well as superior separation and transfer of photogenerated electron–hole pairs in SnO_2@C/CN samples, especially in SnO_2@C/CN-2. Nyquist plots obtained from the electrochemical impedance spectra (EIS) at open circuit potential indicate much smaller charge transfer resistance for SnO_2@C/CN samples compared with g-C_3N_4 (**Fig. 4b**). The incorporation of SnO_2@C promotes the conductivity and thus electron transfer rate in the composite. Photoluminescence (PL) originates from the

recombination of photoinduced electron–hole pairs, which is essential for revealing the separation and transformation of photogenerated charge carriers. Compared with pristine g-C_3N_4, the SnO_2@C/CN heterostructures exhibit a lower intensity PL peak (**Fig. 4c**), indicating suppressed radiative recombination of photogenerated charge carriers owing to the presence of SnO_2@C QDs. The optimized SnO_2@C/CN-2 heterostructure displays the lowest PL intensity, which indicates its superior capability in preventing the recombination of photogenerated charge carriers. Moreover, the transfer dynamics of photogenerated charge carriers was revealed by collecting time-resolved PL (TRPL) spectra as shown in **Fig. 4d**. The photogenerated charge carriers in SnO_2@C/CN-2 have a longer lifetime of 8.75 ns compared with those in g-C_3N_4 (8.5 ns). Such an elongated lifetime of photogenerated electrons in the excited state is highly desirable for subsequent surface reaction.

The impact of SnO_2@C/CN heterostructure formation was investigated by conducting visible-light-driven (λ > 400 nm) photocatalytic hydrogen evolution reaction (HER) using triethanolamine (TEOA) as a sacrificial electron donor to quench the holes generated from bandgap excitation. As displayed in **Fig. 5a** and **5b**, with the assistance of 3 wt.% Pt, SnO_2@C/CN-1, SnO_2@C/CN-2, and SnO_2@C/CN-3 achieve HER rates of 1,018.4, 2,544.3, and 1,446.7 μmol g^{-1} h^{-1}, respectively, which are considerably higher than that of pristine g-C_3N_4 (504.7 μmol g^{-1} h^{-1}). In particular, the SnO_2@C/CN-2 shows an impressive HER rate that is over five-fold enhancement from that of pristine g-C_3N_4. A similar trend is observed even in the absence of Pt co-catalyst. Photocatalytic HER rates of 109.6, 221.7, 490.8, and 295.1 μmol g^{-1} h^{-1} are recorded for pristine g-C_3N_4, SnO_2@C/CN-1, SnO_2@C/CN-2, and SnO_2@C/CN-3, respectively (**Fig. 5b**). The champion HER rate of SnO_2@C/CN-2 is 4.5 times higher than that

of pristine g-C_3N_4. The g-C_3N_4 in the SnO_2@C/CN composites provides a large surface area for supporting the SnO_2@C QDs, which leads to an increased number of active sites for H^+ adsorption and reduction. The interfacial interaction between g-C_3N_4 and SnO_2@C also plays a significant role in enhancing the separation of charges and thus boosting catalytic performance. For comparison, the SnO_2 QDs without carbon encapsulation were prepared and coupled with g-C_3N_4 (SnO_2/CN). Without carbon encapsulation, the SnO_2 QDs tend to aggregate to a 2D layer structure when coupled with g-C_3N_4 (**Fig. S9**). Compared with the SnO_2@C/CN, the SnO_2/CN records much lower photocatalytic HER rates of 766.5 and 154.9 μmol g^{-1} h^{-1} with and without Pt co-catalyst, respectively (**Fig. S10**). This further confirms the important role of carbon layer in the enhancement of photocatalytic activity.

To gain better insights into the photocatalytic property of SnO_2@C/CN-2, apparent quantum efficiency (AQE) was measured under various monochromatic light irradiations (**Fig. 5c**). The AQE values obtained with the irradiations at 420, 425, 435, 475, and 550 nm are 9.63, 4.67, 3.41, 1.78, and 0.31 %, respectively. In a long-term photocatalytic HER test of five consecutive 5 h-runs without fresh addition of TEOA, the SnO_2@C/CN-2 also shows stable performances (**Fig. 5d**). No apparent loss of catalytic activity is observed during whole 25-h reaction, demonstrating an excellent photostability of SnO_2@C/CN-2.

The optical properties of SnO_2@C/CN were investigated to understand the photocatalytic mechanism. UV–vis diffuse reflectance spectra (DRS, **Fig. S11**) indicate that the absorption edge of SnO_2@C/CN-2 is significantly shifted toward the visible region compared with those of SnO_2 QDs and g-C_3N_4. Because the visible absorption of g-C_3N_4 or SnO_2 QDs is very limited or negligible, such enhanced visible light responsivity is believed to arise from the absorption

of carbon that encompasses the SnO_2 QDs. This is supported by the strong visible light absorption of SnO_2@C NSs that are composed of SnO_2 QDs embedded in carbon nanosheets. Based on the Tauc plots obtained using the DRS data (**Fig. 6a**), the band gap energies (E_g) of SnO_2 QDs and g-C_3N_4 are estimated to be 3.80 and 2.74 eV, respectively. Because semiconductors of band gap larger than *ca*. 3.10 eV could not be stimulated, only g-C_3N_4 would produce photon-generated charge carriers. On the other hand, ultraviolet photoelectron spectra (UPS) indicate that the E_{cutoff} (the energy at which the secondary photoemission begins) for SnO_2 QDs and g-C_3N_4 are 16.42 and 16.29 eV, respectively (**Fig. 6b**). The corresponding electron work functions (Φ) are then calculated as 4.80 and 4.93 eV using Equation (3) [53]. The Fermi levels (E_F), as the negative values of Φ, are estimated to be −4.80 and −4.93 eV for SnO_2 QDs and g-C_3N_4, respectively. The valence band energy relative to the vacuum level can be thereby determined by adding the values of VB_{XPS} (the lower emission onset energy) to the Φ, as shown in Equation (4) [54]. By extrapolating the left slope of VB_{XPS} spectra to the baseline, the VB_{XPS} are obtained as 3.24 and 1.77 eV for SnO_2 QDs and g-C_3N_4, respectively (**Fig. 6c**). Overall, the valence band energy (E_{VB}) is calculated as −8.04 and −6.70 eV (against the vacuum level) for SnO_2 QDs and g-C_3N_4, respectively. Thus, the conduction band potentials (E_{CB}) are then determined as −4.24 and −3.96 eV for SnO_2 QDs and g-C_3N_4, respectively, according to Equation (5).

$$\Phi = 21.22 - E_{cutoff} \quad (3)$$

$$E_{VB} = -(\Phi + VB_{XPS}) \quad (4)$$

$$E_{CB} = E_{VB} - E_g \quad (5)$$

Based on the above calculations, band gap alignment and the corresponding photocatalytic

HER mechanism of the SnO_2@C/CN heterostructure are proposed in **Fig. 6d**. Before the composite formation, the SnO_2 QDs show a smaller work function than g-C_3N_4 (**Fig. 6d**, left), and when SnO_2 QDs and g-C_3N_4 are in close contact, the electrons in SnO_2 QDs spontaneously move to g-C_3N_4 across the interface until their Fermi levels are matched. During this process, the carbon layer encapsulating the SnO_2 QDs surface facilitates the electron transfer. As a result, the SnO_2 QDs lose electrons and get positively charged, while the g-C_3N_4 receives electrons and becomes negatively charged at the interface (**Fig. 6d**, middle). Consequently, an interfacial electric field is developed with a direction from SnO_2 QDs to g-C_3N_4, which is consistent with the XPS results. Density functional theory (DFT) calculations presented in **Fig. S12** support the as-formed energy band structures of SnO_2 QDs and g-C_3N_4. In consistent with experimental observations, the computed work function of SnO_2 QDs (110) (4.37 eV) is smaller than that of g-C_3N_4 (002) (4.61 eV, **Fig. S13**), which clearly suggests that the electron would flow from SnO_2 QDs to g-C_3N_4 when they are in contact. Such a built-in electric field at the interface can provide the driving force for efficient charge separation and transfer upon the formation of type II heterostructure (**Fig. 6d**, right). Under illumination, the photoexcited electrons in the conduction band (CB) of g-C_3N_4 are transferred to the CB of the SnO_2 QDs (acting as an electron collector) through the carbon layer on the SnO_2 QDs (acting as a bridge) for the surface reaction. Furthermore, the Pt nanoparticles loaded on the SnO_2 QD surface (**Fig. S14**), owing to their strong electron-withdrawing property, quickly capture the photogenerated electrons from SnO_2 QDs and reduce H^+ to H_2. On the other hand, since the SnO_2 QDs cannot be excited under visible light irradiation, the holes on the valence band (VB) of g-C_3N_4 integrate with the adsorbed sacrificial agent (TEOA), leading to an effective photogenerated electrons–holes

separation. Owing to the extensive and intimate interface that spurs strong electronic coupling between the components, the SnO_2@C/CN architecture ensures an enlarged surface area for efficient surface catalytic reaction and provides a strong driving force for charge transfer, contributing to the fast surface reaction kinetics and exceptional hydrogen evolution performance.

4. Conclusions

In summary, a 0D/2D heterostructure of SnO_2@C/CN has been successfully constructed and demonstrated an exceptional photocatalytic HER performance with an H_2 production rate of 2,544.3 μmol h^{-1} g^{-1}, apparent quantum efficiency of 9.63 % at λ = 420 nm, and excellent cycling stability. Such highly enhanced photocatalytic activities could be ascribed to the synergistic effect among the SnO_2 QDs, carbon, and g-C_3N_4. In particular, the carbon encapsulation stabilizes the SnO_2 QDs and strengthen the interaction between SnO_2 QDs and g-C_3N_4 nanosheets. The built-in electric field at the interface of SnO_2@C/CN drives the efficient separation and transfer of charges, which could significantly extend the lifetime of electron–hole pairs to enhance photocatalytic HER performances. This study demonstrates an effective strategy of constructing a heterostructure for the improvement of photocatalytic H_2 production efficiency, a strategy that could be applied to the designing of other highly active photocatalysts.

Acknowledgement

We gratefully acknowledge the financial supports from the Innovation and Technology Commission of Hong Kong and The Hong Kong Polytechnic University (1-BE0Y). J. Y. acknowledges the support from Postdoctoral Fellowships Scheme from the Hong Kong Polytechnic University (1-YW3J) and Natural Science Foundation of Jiangsu Province (BK20180887).

Appendix A. Supplementary data

Supplementary data to this article can be found online at https://doi.org/xx.xxx/j.cej.2021.xxxxx.

Conflict of Interest

The authors declare no conflict of interest.

References

[1] R. Godin, Y.O. Wang, M.A. Zwijnenburg, J.W. Tang, J.R. Durrant, Time-resolved spectroscopic investigation of charge trapping in carbon nitrides photocatalysts for hydrogen generation, J. Am. Chem. Soc. 139 (2017) 5216-5224.

[2] L.F. Cui, J.L. Song, A.F. McGuire, S.F. Kang, X.Y. Fang, J.J. Wang, C.C. Yin, X. Li, Y.G. Wang, B.X. Cui, Constructing highly uniform onion-ring-like graphitic carbon nitride for efficient visible-light-driven photocatalytic hydrogen evolution, ACS Nano 12 (2018) 5551-5558.

[3] Y.T. Xiao, G.H. Tian, W. Li, Y. Xie, B.J. Jiang, C.G. Tian, D.Y. Zhao, H.G. Fu, Molecule self-assembly synthesis of porous few-layer carbon nitride for highly efficient photoredox catalysis, J. Am. Chem. Soc. 141 (2019) 2508-2515.

[4] L. Kong, Y. Ji, Z. Dang, J. Yan, P. Li, Y. Li, S.F. Liu, g-C_3N_4 loading black phosphorus quantum dot for efficient and stable photocatalytic H_2 generation under visible light, Adv. Funct. Mater. 28 (2018) 1800668.

[5] H. Gao, H. Yang, J. Xu, S. Zhang, J. Li, Strongly coupled g-C_3N_4 nanosheets-Co_3O_4 quantum dots as 2D/0D heterostructure composite for peroxymonosulfate activation, Small 14 (2018) 1801353.

[6] B. Lin, Z. Chen, P. Song, H. Liu, L. Kang, J. Di, X. Luo, L. Chen, C. Xue, B. Ma, G. Yang, J. Tang, J. Zhou, Z. Liu, F. Liu, A tandem 0D/2D/2D NbS_2 quantum dot/Nb_2O_5 nanosheet/g-C_3N_4 flake system with spatial charge-transfer cascades for boosting photocatalytic hydrogen evolution, Small 16 (2020) 2003302.

[7] J.R. Ran, W.W. Guo, H.L. Wang, B.C. Zhu, J.G. Yu, S.Z. Qiao, Metal-free 2D/2D phosphorene/g-C_3N_4 Van der Waals heterojunction for highly enhanced visible-light photocatalytic H_2 production, Adv. Mater. 30 (2018) 1800128.

[8] Y.G. Wang, Q.N. Xia, X. Bai, Z.G. Ge, Q. Yang, C.C. Yin, S.F. Kang, M.D. Dong, X. Li, Carbothermal activation synthesis of 3D porous g-C_3N_4/carbon nanosheets composite with superior performance for CO_2 photoreduction, Appl. Catal., B 239 (2018) 196-203.

[9] Y.N. Liu, Z.F. Shen, J.L. Song, H.L. Qi, C.C. Yin, X.H. Zou, Q.N. Xia, L.F. Cui, X. Li, Y.G. Wang, Honeycomb-like g-C_3N_4/CeO_{2-x} nanosheets obtained *via* one step hydrothermal-roasting for efficient and stable Cr (VI) photo-reduction, Chinese Chemical. Lett. 31 (2020) 2747-2751.

[10] C. Li, Y. Du, D. Wang, S. Yin, W. Tu, Z. Chen, M. Kraft, G. Chen, R. Xu, Unique P-Co-N surface bonding states constructed on g-C_3N_4 nanosheets for drastically enhanced photocatalytic activity of H_2 evolution, Adv. Funct. Mater. 27 (2017) 1604328.

[11] L. Jing, R. Zhu, D.L. Phillips, J.C. Yu, Effective prevention of charge trapping in graphitic carbon nitride with nanosized red phosphorus modification for superior photo(electro)catalysis, Adv. Funct. Mater. 27 (2017) 1703484.

[12] J. Chen, C.L. Dong, D.M. Zhao, Y.C. Huang, X.X. Wang, L. Samad, L.N. Dang, M. Shearer, S.H. Shen, L.J. Guo, Molecular design of polymer heterojunctions for efficient solar-hydrogen conversion, Adv. Mater. 29 (2017) 1606198.

[13] Z. Guo, F. Ambrosio, A. Pasquarello, Evaluation of photocatalysts for water splitting through combined analysis of surface coverage and energy-level alignment, ACS Catal. 10 (2020) 13186-13195.

[14] K. Wang, Y. Li, J. Li, G.K. Zhang, Boosting interfacial charge separation of $Ba_5Nb_4O_{15}$/g-C_3N_4 photocatalysts by 2D/2D nanojunction towards efficient visible-light driven H_2 generation, Appl. Catal., B 263 (2020) 117730.

[15] W. Chen, Z.-C. He, G.-B. Huang, C.-L. Wu, W.-F. Chen, X.-H. Liu, Direct Z-scheme 2D/2D $MnIn_2S_4$/g-C_3N_4 architectures with highly efficient photocatalytic activities towards treatment of pharmaceutical wastewater and hydrogen evolution, Chem. Eng. J. 359 (2019) 244-253.

[16] Y.L. Chen, F.Y. Su, H.Q. Xie, R.P. Wang, C.H. Ding, J.D. Huang, Y.X. Xu, L.Q. Ye, One-step construction of S-scheme heterojunctions of N-doped MoS_2 and S-doped g-C_3N_4 for enhanced photocatalytic hydrogen evolution, Chem. Eng. J. 404 (2021) 126498.

[17] J. Cui, S. Yao, J.-Q. Huang, L. Qin, W.G. Chong, Z. Sadighi, J. Huang, Z. Wang, J.-K. Kim, Sb-doped SnO_2/graphene-CNT aerogels for high performance Li-ion and Na-ion battery anodes, Energy Stor. Mater. 9 (2017) 85-95.

[18] B. Ahmed, D.H. Anjum, Y. Gogotsi, H.N. Alshareef, Atomic layer deposition of SnO_2 on MXene for Li-ion battery anodes, Nano Energy 34 (2017) 249-256.

[19] S. Byun, B. Shin, Densely packed hybrid films comprising SnO_2 and reduced graphite oxide for high-density electrochemical capacitors, J. Mater. Chem. A 4 (2016) 16175-16183.

[20] K. Deng, Q. Chen, L. Li, Modification engineering in SnO_2 electron transport layer toward perovskite solar cells: efficiency and stability, Adv. Funct. Mater. 30 (2020) 2004209.

[21] J. Wei, F. Guo, X. Wang, K. Xu, M. Lei, Y. Liang, Y. Zhao, D. Xu, SnO_2-in-polymer matrix for high-efficiency perovskite solar cells with improved reproducibility and stability, Adv. Mater. 30 (2018) 1805153.

[22] D. Yang, R. Yang, K. Wang, C. Wu, X. Zhu, J. Feng, X. Ren, G. Fang, S. Priya, S.F. Liu, High efficiency planar-type perovskite solar cells with negligible hysteresis using EDTA-complexed SnO_2, Nat. Commun. 9 (2018) 3239.

[23] D. Liu, Y. Wang, H. Xu, H. Zheng, T. Zhang, P. Zhang, F. Wang, J. Wu, Z. Wang, Z. Chen, S. Li, SnO_2-based perovskite solar cells: configuration design and performance improvement, Solar RRL 3 (2019) 1800292.

[24] Z. Song, S. Xu, J. Liu, Z. Hu, N. Gao, J. Zhang, F. Yi, G. Zhang, S. Jiang, H. Liu, Enhanced catalytic activity of SnO_2 quantum dot films employing atomic ligand-exchange strategy for fast response H_2S gas sensors, Sens. Actuators, B. 271 (2018) 147-156.

[25] Z. Song, Z. Wei, B. Wang, Z. Luo, S. Xu, W. Zhang, H. Yu, M. Li, Z. Huang, J. Zang, F. Yi, H. Liu, Sensitive room-temperature H_2S gas sensors employing SnO_2 quantum wire/reduced graphene oxide nanocomposites, Chem. Mater. 28 (2016) 1205-1212.

[26] H. Liu, H. Li, L. Gao, J. Tang, Colloidal quantum dots for low-power-consumption semiconductor gas sensors, Proceedings 26 (2019) 22.

[27] K. Chu, Y.P. Liu, Y.B. Li, J. Wang, H. Zhang, Electronically coupled SnO_2 quantum dots and graphene for efficient nitrogen reduction reaction, ACS Appl. Mater. Interfaces 11 (2019) 31806-31815.

[28] X. Wang, H. Fan, P. Ren, Electrospinning derived hollow SnO_2 microtubes with highly photocatalytic property, Catal. Commun. 31 (2013) 37-41.

[29] A. Zada, M. Khan, M.N. Qureshi, S.Y. Liu, R. Wang, Accelerating photocatalytic hydrogen production and pollutant degradation by functionalizing g-C_3N_4 with SnO_2, Front. Chem. 7 (2019) 941.

[30] Y. Zang, L. Li, X. Li, R. Lin, G. Li, Synergistic collaboration of g-C_3N_4/SnO_2 composites for enhanced visible-light photocatalytic activity, Chem. Eng. J. 246 (2014) 277-286.

[31] D. Li, J. Huang, R. Li, P. Chen, D. Chen, M. Cai, H. Liu, Y. Feng, W. Lv, G. Liu, Synthesis of a carbon dots modified g-C_3N_4/SnO_2 *Z*-scheme photocatalyst with superior photocatalytic activity for ppcps degradation under visible light irradiation, J. Hazard. Mater. 401 (2020) 123257.

[32] K. Zhu, Y. Lv, J. Liu, W. Wang, C. Wang, S. Li, P. Wang, M. Zhang, A. Meng, Z. Li, Facile fabrication of g-C_3N_4/SnO_2 composites and ball milling treatment for enhanced photocatalytic performance, J. Alloys Compd. 802 (2019) 13-18.

[33] Y. Chen, W. Li, D. Jiang, K. Men, Z. Li, L. Li, S. Sun, J. Li, Z.-H. Huang, L.-N. Wang, Facile synthesis of bimodal macroporous g-C_3N_4/SnO_2 nanohybrids with enhanced photocatalytic activity, Sci. Bull. 64 (2019) 44-53.

[34] L. Yang, J. Huang, L. Shi, L. Cao, H. Liu, Y. Liu, Y. Li, H. Song, Y. Jie, J. Ye, Sb doped SnO_2-decorated porous g-C_3N_4 nanosheet heterostructures with enhanced photocatalytic activities under visible light irradiation, Appl. Catal., B 221 (2018) 670-680.

[35] C. Fettkenhauer, G. Clavel, K. Kailasam, M. Antonietti, D. Dontsova, Facile synthesis of new, highly efficient SnO_2/carbon nitride composite photocatalysts for the hydrogen evolution reaction, Green Chem. 17 (2015) 3350-3361.

[36] D. Zhang, B. Mao, D. Li, Y. Liu, F. Li, W. Dong, T. Jiang, W. Shi, 0D/2D Z-scheme heterojunctions of Zn-$AgIn_5S_8$ QDs/α-Fe_2O_3 nanosheets for efficient visible-light-driven hydrogen production, Chem. Eng. J. 417 (2021) 128275.

[37] U.P. Suryawanshi, U.V. Ghorpade, D.M. Lee, M.He, S.W. Shin, P.V. Kumar, J.S. Jang, H.R. Jung, M.P. Suryawanshi, M.P. Suryawanshi, Colloidal Ni_2P nanocrystals encapsulated in heteroatom-doped graphene nanosheets: a synergy of 0D@2D heterostructure toward overall water splitting. Chem. Mater. 33 (2021) 234-245.

[38] P.F. Xia, S.W. Cao, B.C. Zhu, M.J. Liu, M.S. Shi, J.G. Yu, Y.F. Zhang, Designing a 0D/2D

S-scheme heterojunction over polymeric carbon nitride for visible-light photocatalytic inactivation of bacteria, Angew. Chem. Int. Ed. 59 (2020) 5218-5225.

[39] Y. Zou, Y. Xie, S. Yu, L. Chen, W. Cui, F. Dong, Y. Zhou, SnO_2 quantum dots anchored on g-C_3N_4 for enhanced visible-light photocatalytic removal of NO and toxic NO_2 inhibition, Appl. Surf. Sci. 496 (2019) 143630.

[40] J. Liu, Q. Zhang, X. Tian, Y. Hong, Y. Nie, N. Su, G. Jin, Z. Zhai, C. Fu, Highly efficient photocatalytic degradation of oil pollutants by oxygen deficient SnO_2 quantum dots for water remediation, Chem. Eng. J. 404 (2021) 127146.

[41] M.T. Hoang, N.D. Pham, J.H. Han, J.M. Gardner, I. Oh, Integrated photoelectrolysis of water implemented on organic metal halide perovskite photoelectrode, ACS Appl. Mater. Interfaces 8 (2016) 11904-11909.

[42] I. Poli, U. Hintermair, M. Regue, S. Kumar, E.V. Sackville, J. Baker, T.M. Watson, S. Eslava, P.J. Cameron, Graphite-protected $CsPbBr_3$ perovskite photoanodes functionalised with water oxidation catalyst for oxygen evolution in water, Nat. Commun. 10 (2019) 10.

[43] S. Jing, J. Lu, G. Yu, S. Yin, L. Luo, Z. Zhang, Y. Ma, W. Chen, P.K. Shen, Carbon-encapsulated WO_x hybrids as efficient catalysts for hydrogen evolution, Adv. Mater. 30 (2018) 1705979.

[44] X. Chen, J. Wang, Y. Chai, Z. Zhang, Y. Zhu, Efficient Photocatalytic Overall water splitting induced by the giant internal electric field of a g-C_3N_4/rGO/PDIP *Z*-Scheme heterojunction, Adv. Mater. 33 (2021) 2007479.

[45] H. Liu, M. Li, O. Voznyy, L. Hu, Q.Y. Fu, D.X. Zhou, Z. Xia, E.H. Sargent, J. Tang, Physically flexible, rapid-response gas sensor based on colloidal quantum dot solids, Adv. Mater. 26 (2014) 2718-2724.

[46] Z.L. Song, J. Yan, J.B. Lian, W.J. Pu, L.Q. Jing, H. Xu, H.M. Li, Graphene oxide-loaded SnO_2 quantum wires with sub-4 nanometer diameters for low-temperature H_2S gas sensing, ACS Appl. Nano Mater. 3 (2020) 6385-6393.

[47] D. Tiwari, D.J. Fermin, T.K. Chaudhuri, A. Ray, Solution processed bismuth ferrite thin films for all-oxide solar photovoltaics, J. Phys. Chem. C 119 (2015) 5872-5877.

[48] L. Gao, G. Wu, J. Ma, T. Jiang, B. Chang, Y. Huang, S. Han, SnO_2 quantum

dots@graphene framework as a high-performance flexible anode electrode for lithium-ion batteries, ACS Appl. Mater. Interfaces 12 (2020) 12982-12989.

[49] G. Zhang, J. Zhang, M. Zhang, X. Wang, Polycondensation of thiourea into carbon nitride semiconductors as visible light photocatalysts, J. Mater. Chem. 22 (2012) 8083-8091.

[50] P. Niu, L. Zhang, G. Liu, H.-M. Cheng, Graphene-like carbon nitride nanosheets for improved photocatalytic activities, Adv. Funct. Mater. 22 (2012) 4763-4770.

[51] L. Shen, F. Liu, G. Chen, H. Zhou, Z. Le, H.B. Wu, G. Wang, Y. Lu, Encapsulation of SnO_2 nanocrystals into hierarchically porous carbon by melt infiltration for high-performance lithium storage, J. Mater. Chem. A 4 (2016) 18706-18710.

[52] S. Li, T. Wang, W. Zhu, J. Lian, Y. Huang, Y.-Y. Yu, J. Qiu, Y. Zhao, Y.-C. Yong, H. Li, Controllable synthesis of uniform mesoporous *h*-Nb_2O_5/rGO nanocomposites for advanced lithium ion hybrid supercapacitors, J. Mater. Chem. A 7 (2019) 693-703.

[53] J. Zhang, D. Bai, Z. Jin, H. Bian, K. Wang, J. Sun, Q. Wang, S. Liu, 3D-2D-0D interface profiling for record efficiency all-inorganic $CsPbBrI_2$ perovskite solar cells with superior stability, Adv. Energy Mater. 8 (2018) 1703246.

[54] Y. Wang, X. Kong, M. Jiang, F. Zhang, X. Lei, A *Z*-scheme $ZnIn_2S_4/Nb_2O_5$ nanocomposite: constructed and used as an efficient bifunctional photocatalyst for H_2 evolution and oxidation of 5-hydroxymethylfurfural, Inorg. Chem. Front. 7 (2020) 437-446.

Figures

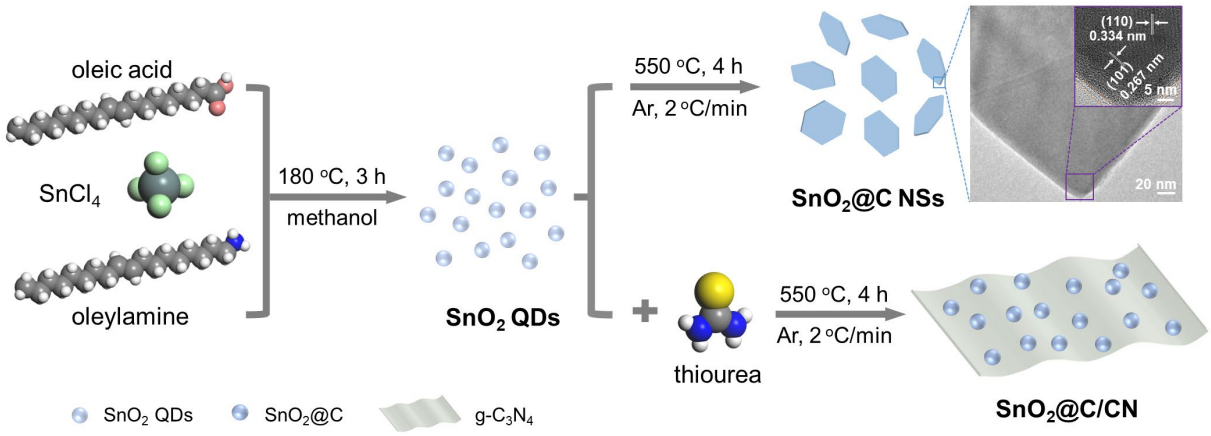

Scheme 1. An overview of synthetic procedure for SnO_2 quantum dots (SnO_2 QDs), carbon-encapsulated SnO_2 nanosheets (SnO_2@C NSs), and carbon-encapsulated SnO_2 QDs-anchored g-C_3N_4 nanosheets (SnO_2@C/CN). TEM image is SnO_2@C NSs.

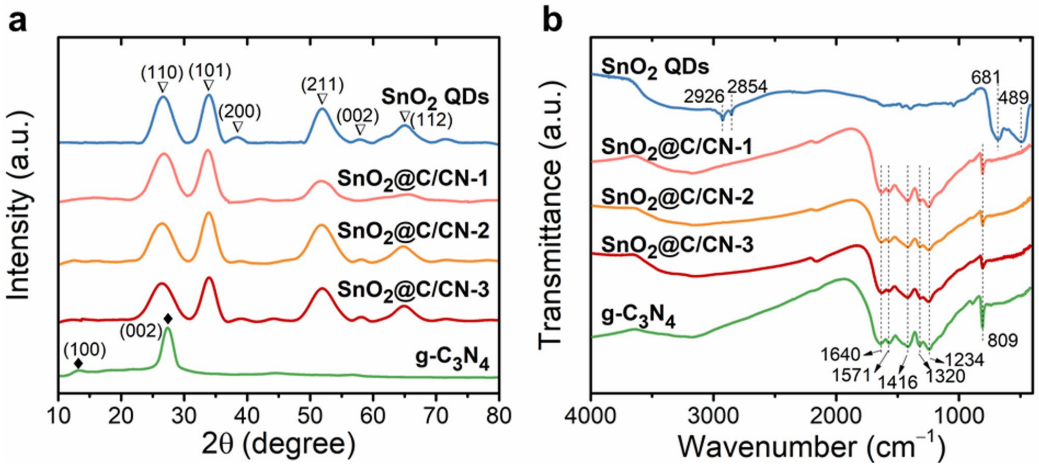

Fig. 1. (a) XRD and (b) FT-IR spectra of SnO_2 QDs, g-C_3N_4, and SnO_2@C/CN composites.

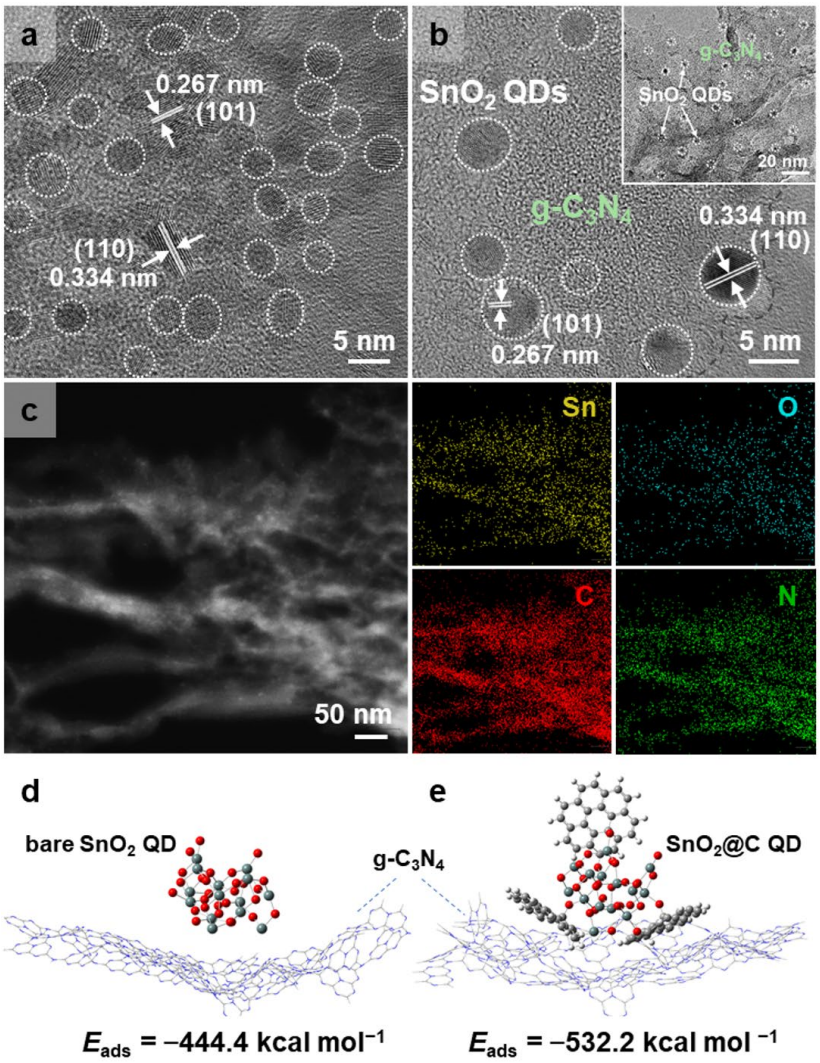

Fig. 2. TEM image of (a) SnO_2 QDs. (b) HRTEM and (c) EDX elemental mapping images of SnO_2@C/CN-2. Inset in (b) is the corresponding TEM image. Side-views of the adsorption configurations of (d) bare SnO_2 and (e) SnO_2@C QDs on g-C_3N_4 surface.

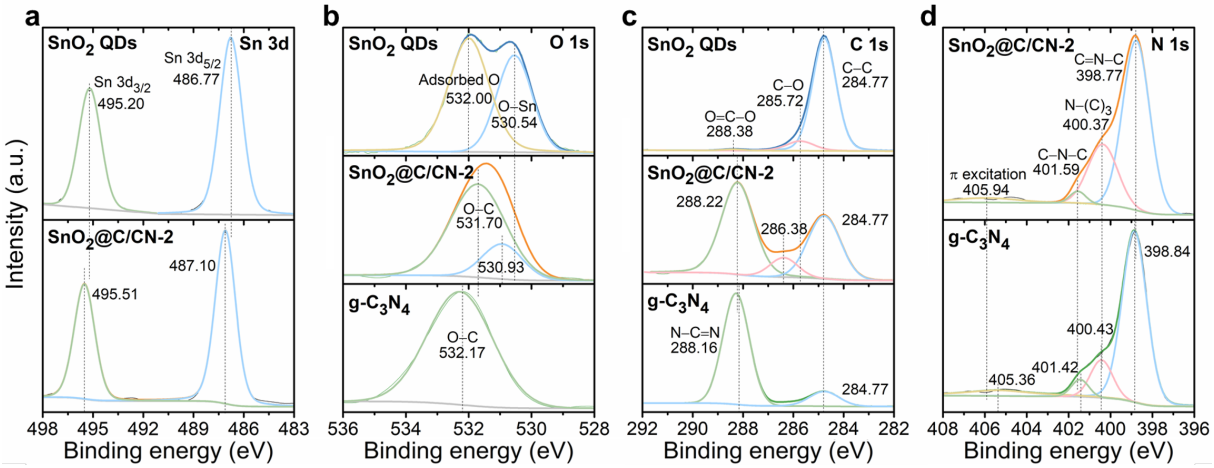

Fig. 3. High-resolution XPS spectra in (a) Sn 3d, (b) O 1s, (c) C 1s, (d) N 1s regions of SnO_2 QDs, g-C_3N_4, and SnO_2@C/CN-2.

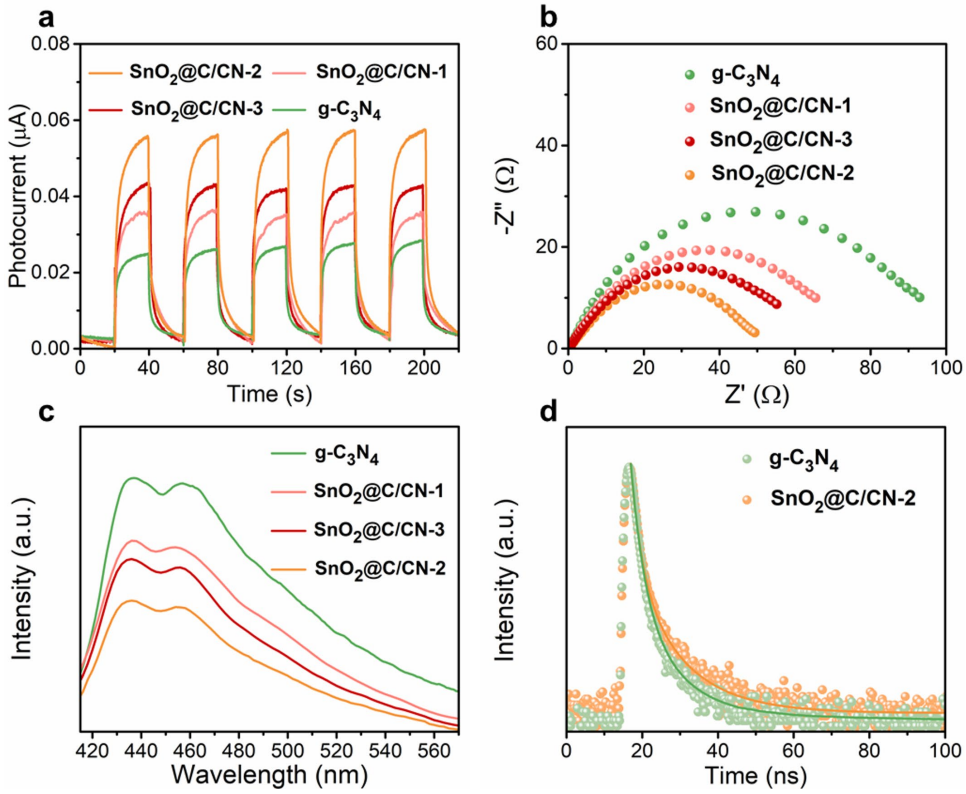

Fig. 4. (a) Photocurrent responses under chopped light illumination, (b) EIS spectra, and (c) PL spectra of SnO_2@C/CN samples and g-C_3N_4. (d) TRPL spectra of SnO_2@C/CN-2 and g-C_3N_4. Photocurrent and EIS were measured at 0 V and open circuit potential, respectively. PL and TRPL were obtained with an excitation wavelength of 325 nm.

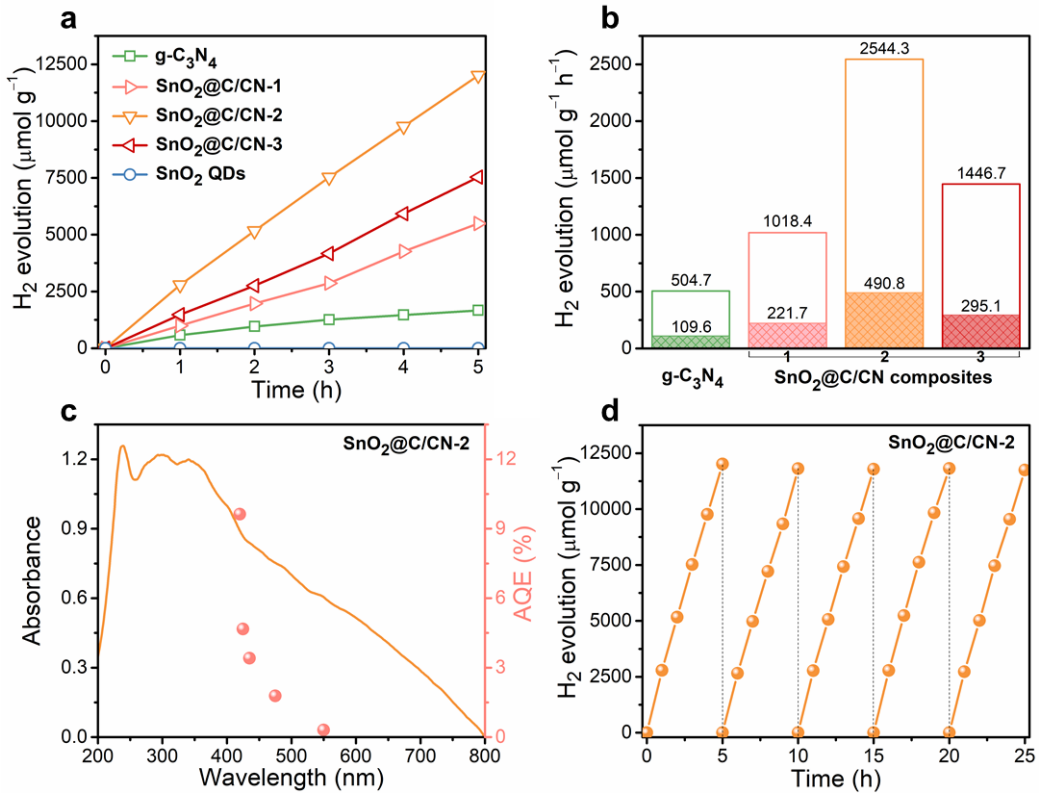

Fig. 5. (a) Photocatalytic H_2 evolution in 5 h and (b) photocatalytic H_2 evolution rate over g-C_3N_4, SnO_2 QDs, and SnO_2@C/CN composites. (c) Wavelength dependence of AQE and (d) long-term photocatalytic H_2 evolution rate of SnO_2@C/CN QDs-2.

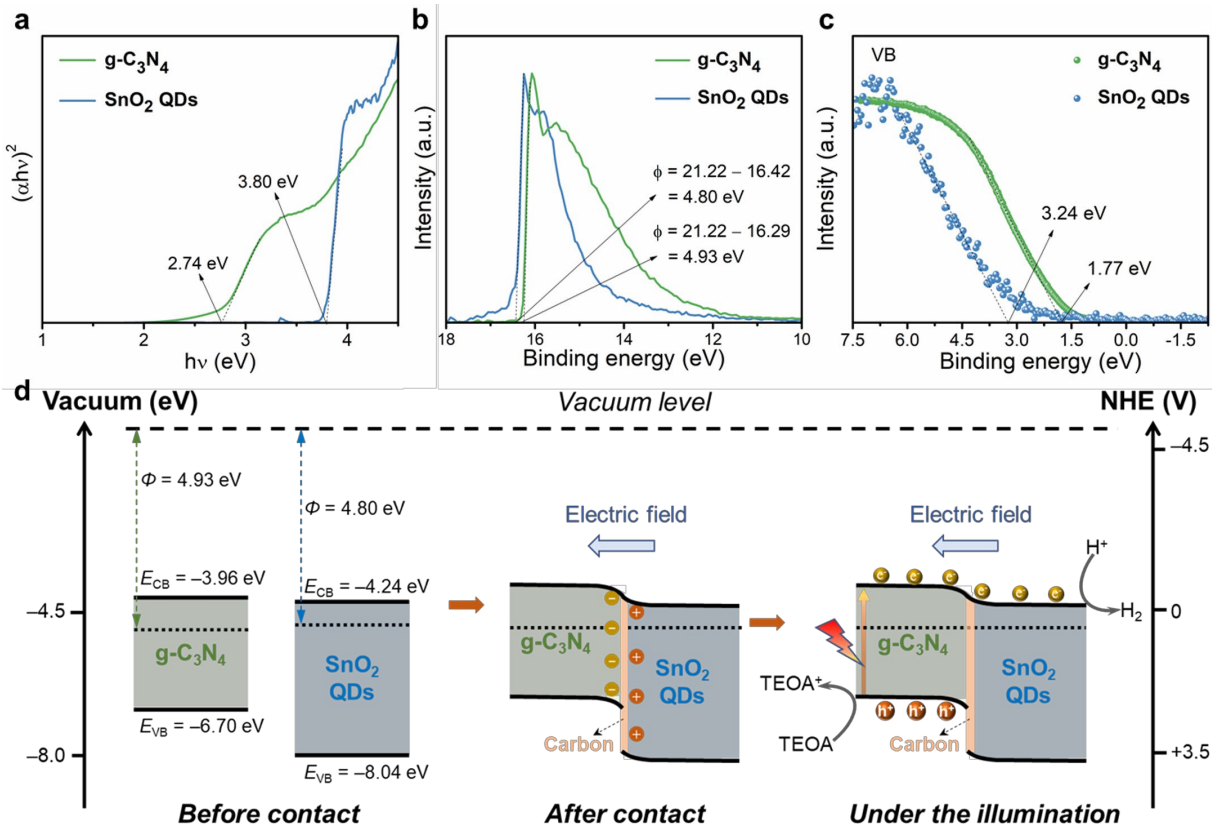

Fig. 6. (a) Tauc plots, (b) UPS spectra, and (c) VB XPS spectra of SnO_2 QDs and g-C_3N_4. (d) Proposed band alignment and mechanism of photocatalytic H_2 evolution involved in the SnO_2@C/CN.